Available online at www.sciencedirect.com
ScienceDirect
Catalysis Today 127 (2007) 70–84
CATALYSIS TODAY
www.elsevier.com/locate/cattod

CoMo/Ti-SBA-15 catalysts for dibenzothiophene desulfurization

R. Nava [a], R.A. Ortega [b], G. Alonso [c], C. Ornelas [c], B. Pawelec [d], J.L.G. Fierro [d,*]

[a] *CFATA, UNAM, Campus UNAM Juriquilla, Querétaro 76000, Mexico*
[b] *Facultad de Química, UNAM, Ciudad Universitaria, 76010 Mexico, Mexico*
[c] *CIMAV, S.C., Complejo Industrial Chihuahua, Chihuahua 3109, Mexico*
[d] *Instituto de Catálisis y Petroleoquímica, CSIC, Cantoblanco, 28049 Madrid, Spain*

Available online 9 April 2007

Abstract

With a view to reducing the sulfur content in diesel fuels, novel desulfurization CoMo catalysts were supported on a Ti-loaded hexagonal mesoporous SBA-15 material. The Ti-SBA-15 substrates were synthesized using triblock copolymers as structure-directing agents. Catalytic activity was assessed in the model reaction of hydrodesulfurization (HDS) of dibenzothiophene (DBT), carried out in a batch reactor at $T = 623$ K and with a total hydrogen pressure of 3.1 MPa. The reaction proceeds via the direct desulfurization route (main route) and the hydrogenation (HYD) pathway. The incorporation of Ti into the SBA-15 afforded catalysts that were more active than the Ti-free counterpart, due to the enhancement of the DDS route in this reaction. This difference was explained in terms of a larger number of coordinately unsaturated sites (CUS) of the metal sulfide on Ti-loaded catalysts. Under steady-state conditions, the CoMoST20 catalyst with a Si/Ti ratio of 20 was the most active among the catalysts studied. Since this catalyst exhibited both Ti^{4+} ions incorporated into the SBA-15 framework and separate anatase TiO_2 clusters located on its surface, the activity enhancement on this sample was explained by the larger intrinsic activity of the ''Co–Mo–S'' phase located on these TiO_2 nanoparticles. The Ti-SBA-15 supports and the CoMo/Ti-SBA-15 catalysts were studied by N_2 adsorption–desorption isotherms, XRD, TEM, FTIR of adsorbed pyridine and NO, UV–vis DRS, TPR, micro-Raman and XPS spectroscopy.

Keywords: CoMo; Ti-SBA-15; MCM-41; CoMo; SBA-15; Dibenzothiophene; Hydrodesulfurization

1. Introduction

Government regulations call for the production and use of more environmentally friendly fuels with lower contents of sulfur and aromatics [1]. Moreover, for syngas and hydrogen production employing fuel cell systems, the sulfur level in fuels such as gasoline and diesel needs to be reduced to 0.01 ppm [2,3]. Calculations indicate that in order to achieve such a low sulfur level, the catalysts must be ca. 7 times more active than existing ones [3]. Thus, the development of highly active and selective hydrodesulfurization (HDS) catalysts is one of the most pressing problems facing the petroleum industry.

Numerous approaches have been adopted with a view to improving the catalytic performance of the classical formulation of a hydrotreating catalyst ($Co(Ni)Mo(W)/Al_2O_3$). Among these, the more important ones are variations in the preparation method, active component and/or support. Regarding new support materials, mesoporous molecular sieves such as MCM-41 [4–9], HMS [10–16] or SBA-15 [9,17–20] are promising candidates because of their uniform mesoporous structure, which facilitates the diffusion of the large molecules involved in HDS and hydrocracking reactions [21,22]. The support effect in the HDS reaction has been analyzed in detail in recent reviews [21,22]. Compared with MCM-41 and HMS, the SBA-15 material synthesized under an acidic medium using neutral organic triblock copolymers as structure-directing agents [23,24] seems to be more interesting. The SBA-15 possesses a high specific area (600–1000 m^2/g), being formed by a hexagonal array of uniform tubular channels with pore diameters ranging from 5.0 to 30.0 nm, which are significantly larger than those of HMS and MCM-41. Compared to HMS and MCM-41, the SBA-15 material has thicker pore walls and better hydrothermal stability, remaining stable for at least 48 h in boiling water [23]. This latter characteristic is very important for hydrotreating processes carried out under severe reaction conditions. Thus, the excellent performance of highly loading

* Corresponding author. Tel.: +34 915 854 769; fax: +34 915 854 760.
E-mail address: jlgfierro@icp.csic.es (J.L.G. Fierro).

0920-5861/$ – see front matter
doi:10.1016/j.cattod.2007.02.034

NiWS/SBA-15 catalysts for deep hydrotreatment of petroleum feedstock's was proven by Vradman et al. [18]. Given the very weak metal-support interaction, the good catalytic response of those systems was due to the specific method of catalyst preparation employed (ultrasonic deposition of WS_2) [18]. Further studies conducted by Murali Dhar et al. [17] revealed that the SBA-15-supported Mo, CoMo and NiMo catalysts record higher activities compared to alumina-supported catalysts prepared in a similar manner, with the CoMo formulation being more effective than unpromoted Mo or the binary NiMo system. Another study performed by Sampieri et al. [9] showed that the effect of Mo loading on the overall HDS of dibenzothiophene depends on the choice of the silica support, with the SBA-15 supported catalysts being more active than MCM-41 supported ones. This was linked to large differences in the structure of these two series of catalysts, as revealed by TEM [9]. As the hydrotreating Mo/TiO_2 catalysts recorded greater intrinsic activity in the HDS reaction than classical Al_2O_3-supported Mo catalysts [25,26], recent studies have focused on the titanium-modified SBA-15(SBA-16) materials [27,28,20]. Moreover, it was found that MoO_3 species supported on TiO_2 were more easily transformed into catalytically active MoS_2 phase due to an enhancement of molybdenum dispersion linked to the high density of hydroxyl groups on the titanium [25,26]. Indeed, our previous study on the CoMo/Ti-HMS catalysts revealed their greater activity compared to a Ti-free sample in an HDS reaction of dibenzothiophene (DBT) and 4-methyl,6-ethyl dibenzothiophene (4M,6E DBT), and this was explained by the stronger metal-support interaction induced by the presence of Ti^{4+} ions incorporated into the HMS framework [12–15]. Similarly, it was found that aluminum or titanium incorporation in the SBA-15 or SBA-16 materials provides better dispersion of Ni and Mo species. Consequently, the Ti-modified NiMo/SBA-15 and NiMo/SBA-16 catalysts show greater activity in the HDS of 4,6-dimethyl DBT than their Ti-free counterparts [25–27].

Major emphasis has been placed on avoiding the formation of anatase TiO_2 phase on the surface of mesoporous silica materials [12–16,25]. Indeed, it was reported that the NiMo/SBA-16 samples modified by Ti, by the post-synthesis impregnation method, showed lower activity than their counterparts modified by grafting because of the presence of the different Ti species, such as isolated Ti species, small anatase clusters located inside the channels of SBA-16 and large anatase crystals located on the external support surface [27]. However, considering the previous studies on TiO_2-supported catalysts [28,20], and if the formation of large TiO_2 clusters is avoided, one might expect the beneficial effect of the presence of small clusters of anatase TiO_2 phase located on the SBA-15 support surface.

Accordingly, the present work sought to analyze the effect of the Ti-modification of pure SBA-15 material on the catalytic behavior of sulfide CoMo/Ti-SBA-15 catalysts in the HDS reaction of DBT. Variable amounts of Ti^{4+} ions (Si/Ti molar ratio of 80, 60, 40 and 20) were incorporated during the direct hydrothermal synthesis of the SBA-15 support. It has been shown that the presence of small clusters of anatase TiO_2 phase located on the catalyst surface together with the presence of Ti^{4+} ions incorporated into the SBA-15 framework are both beneficial factors for catalyst activity in an HDS reaction. The activity test has been performed in a batch reactor at 623 K and with a hydrogen pressure of 3.1 MPa, and catalytic activity has been compared to that of a conventional commercial $CoMo/Al_2O_3$ catalyst. In order to obtain a catalyst activity–structure correlation, the synthesized pure supports and CoMo catalysts were characterized by different techniques.

2. Experimental

2.1. Support/catalyst preparation

The siliceous SBA-15 mesoporous material was synthesized according to the procedure described by Flodström and Alfredsson [29], using Pluronic triblock copolymer (BASF, EO_{20}-PO_{70}-EO_{20}, P123) as the structure-directing agent and tetraethyl orthosilicate (TEOS, 98%, Aldrich) as a source of silica. In a typical synthesis, the triblock copolymer was dissolved in a solution of water and HCl under stirring, after which the required amount of TEOS was added to the solution at 308 K and kept under stirring conditions for 24 h. The mixture was subsequently transferred into polypropylene bottles and heated at 358 K for 24 h. After synthesis, the solid obtained was filtered, washed thoroughly with distilled water, dried at 373 K and finally calcined at 773 K for 6 h to remove the organic template. The titanium-containing SBA-15 mesoporous materials were synthesized using the same procedure as for the SBA-15 material, except for dissolving the appropriate amounts of titanium (IV) butoxide (97%, Aldrich) in TEOS in order to obtain samples with Si/Ti molar ratios of 80, 60, 40 and 20.

A series of CoMo catalysts was prepared using the Ti-free and Ti-loaded SBA-15 substrates. Each support was loaded with fixed amounts of molybdenum (10 wt.%) and cobalt (3 wt.%) by consecutive incipient wet impregnation (Mo being introduced first) from solutions of ammonium heptamolybdate tetrahydrate (Aldrich, A.C.S. reagent) and cobalt (II) nitrate hexahydrate (Aldrich, 98%) to achieve a Co:Mo molar ratio of 1:3. After impregnation, the samples were dried overnight at 383 K in air and then calcined for 3 h at 773 K, also in air. The CoMo/SBA-15 and CoMo/Ti-SBA-15 catalysts are henceforth referred to as CoMoST*x*, where *x* denotes the Si/Ti molar ratios (∞, 80, 60, 40 and 20).

2.2. Catalyst/support characterization

The textural properties of the calcined catalysts were measured by isothermal adsorption of nitrogen at 77 K with a Micromeritics TriStar 3000 apparatus. The samples were previously degassed at 423 K for 24 h under a vacuum (10^{-4} mbar) to ensure a clean dry surface, free of any loosely bound adsorbed species. The specific areas of the samples were determined according to standard BET procedure using nitrogen adsorption data collected in the relative equilibrium pressure interval of $0.03 < P/P^0 < 0.3$. Pore size distributions were calculated from the adsorption and desorption branches of the corresponding nitrogen isotherm using the BJH method.

The total pore volume (V_p) was estimated from the amount of nitrogen adsorbed at a relative pressure of 0.98, and the micropore volume (V_μ) and the micropore area (S_μ) were estimated using the *t*-plot method.

Powder X-ray diffraction (XRD) measurements for structural determinations were recorded using Cu Kα radiation in the 2θ range of 0.5–80° on a DMAX 2100 Rigaku diffractometer. Transmission electron microscopy (TEM) studies were carried out using a JEOL JEM 2000FX microscope operating at 200 kV with very low illumination in order to avoid the destruction of material under the electron beam. The calcined catalysts were crushed and dispersed ultrasonically in acetone at room temperature and then spread onto a perforated carbon–copper microgrid.

UV–vis diffuse reflectance spectra of the oxide catalysts were recorded in the 200–700 nm range at room temperature, using a Varian Cary 3 UV–vis spectrometer equipped with an integration sphere. The respective support in each catalyst was used as reference.

Micro-Raman spectra were recorded in a commercial micro-Raman system (Dilor Labram model) equipped with a 20 mW He–Ne laser emitting at 632.8 nm, and a holographic notch filter from Kaiser Optical Systems, Inc. (model SuperNotch-Plus). All Raman spectra were recorded at room temperature. TPR experiments were conducted on a Micromeritics 2900 device fitted with a TCD and interfaced to a data station. Prior to reduction, the catalysts (ca. 50 mg) were heated at a rate of 15 K/min to a final temperature of 673 K, and kept for 2 h at that temperature under a He flow to remove water and other contaminants. The catalysts were cooled to ambient temperature in the same He flow, reduced in flowing gas containing 10 vol.% H_2 in Ar at a total flow rate of 50 mL/min, and finally heated at a rate of 15 K/min to a final temperature of 1300 K.

The X-ray photoelectron spectra of the fresh sulfided (673 K for 4 h) catalysts were recorded to determine the relative dispersion and the degree of sulfidation of the supported species. A VG Escalab 200R spectrometer equipped with a hemispherical electron analyzer and a Mg Kα ($h\nu$ = 1253.6 eV) X-ray source was used. The samples were first placed in a copper holder mounted on a sample-rod in the pretreatment chamber of the spectrometer, and then degassed at 403 K for 1 h before transfer to the analysis chamber. The freshly sulfided CoMo catalysts were kept under *i*-octane in order to avoid exposure to air, being subsequently placed in the preparation chamber. All the catalysts were degassed at 10^{-5} mbar and then transferred to the ion-pumped analysis chamber, where residual pressure was kept below 7×10^{-9} mbar during data acquisition. The binding energies (BE) were referenced to the C 1s peak (284.9 eV) to account for the charging effects. The areas of the peaks were computed after fitting the experimental spectra to Gaussian/Lorentzian curves and removing the background (Shirley function). Surface atomic ratios were calculated from the peak area ratios normalized by the corresponding atomic sensitivity factors [30].

The acidity of the sulfided catalysts was monitored by the FTIR of adsorbed pyridine. After sulfidation at 673 K, the samples were degassed at 723 K for 0.5 h and cooled to ambient temperature prior to contact with ca. 2 mbar of pyridine. Physically adsorbed pyridine was removed by degassing at 393 K for 1 h.

The FTIR spectroscopy of adsorbed NO was used to measure the dispersion and sulfidation degree of the supported metal species after *in situ* sulfidation at 673 K. Self-supporting wafers of the catalysts with thickness of 12 mg cm^{-2} were prepared by pressing the powdered samples at a pressure of 7×10^3 kg cm^{-2} for 10 min. The samples were degassed at 673 K for 2 h in a special IR cell with greaseless stopcocks and KBr windows. Once the samples were cooled to ambient temperature, they were exposed to 20 mbar of NO for 5 min and the spectrum was subsequently recorded on a Nicolet 510 FTIR spectrophotometer at a resolution of 4 cm^{-1}. The sample was then degassed at 673 K for 2 h to achieve total desorption of the NO molecules, and the spectrum of the catalyst was recorded. The IR spectrum of the adsorbed NO was obtained by subtracting the spectrum of the corresponding catalyst degassed at 673 K.

2.3. Activity measurements

Both the synthesized catalysts and a commercial CoMo/Al_2O_3 one, used as reference, were tested in a dibenzothiophene HDS reaction carried out in a Parr model 4522 high-pressure batch reactor. Reaction conditions were: T = 623 K, total hydrogen pressure of 3.1 MPa and a reaction time of 5 h. Prior to the catalytic test, the catalysts were sulfided at 673 K for 4 h under a H_2/H_2S gas flow (15% H_2S, v/v) at atmospheric pressure with a heating rate of 4 K/min. The catalyst (1 g; particle size in range 0.20–0.35 mm) was fed into the reactor with the reagent mixture (6.6 g of DBT in 150 mL of decalin; $[DBT]_o$ = 0.239 mol/L). The reactor was pressurized to 3.1 MPa with hydrogen and then heated to 623 K at a rate of 10 K/min. The stirring of the reaction mixture was sufficiently intense to exclude external diffusion limitations (checked by varying the amount of catalyst and the stirring rate (1000, 800 and 700 rpm)). Samples were taken for chromatographic analysis during the course of each run in order to determine conversion *versus* time dependence. The reaction products were analyzed using a Perkin-Elmer Auto-system chromatograph with a 9 ft, 1/8 in. packed column containing chromosorb W-AW 80/100 mesh 3% OV-17 (phenyl methyl silicone 50% phenyl) as a separating phase. The mean standard deviation for catalytic measurements was about 3%. The comparison of selectivity was made for the catalysts showing the same DBT conversion (ca. 30%) at different reaction time.

3. Results

3.1. Characterization of oxide catalysts

The textural properties of the oxide CoMo/SBA-15 catalysts with and without Ti were studied by means of nitrogen adsorption–desorption isotherms measured at 77 K, small-angle X-ray diffraction and TEM techniques. Fig. 1A and B presents the nitrogen adsorption–desorption isotherms and the

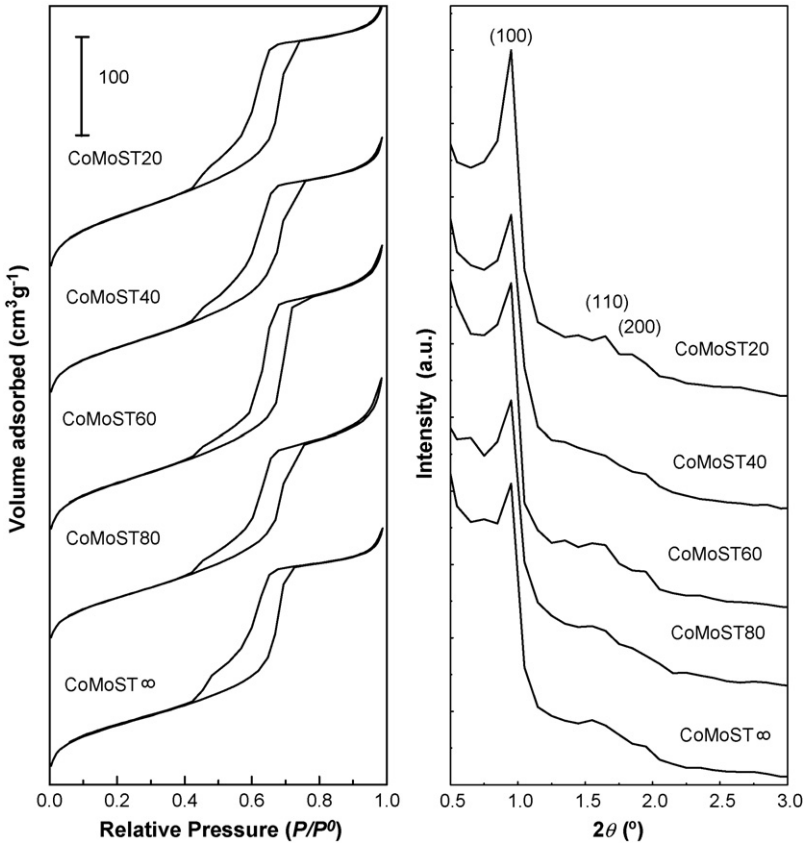

Fig. 1. N_2 adsorption–desorption isotherms at 77 K together with the corresponding small-angle X-ray diffraction patterns for a series of the oxide CoMo/SBA-15 catalysts with and without of Ti.

corresponding small-angle XRD patterns, respectively. As can be seen from Fig. 1A, the samples studied show type IV adsorption isotherms with the H1-type hysteresis loop and all isotherms are similar to that reported in literature for SBA-15 mesoporous material [18,27]. The H1-type hysteresis loop of nitrogen isotherms is characteristic of a percolation effect caused by small particles of the metal oxides being located within the mesopores, forming ink-bottle type pores [31,32]. The small-angle XRD patterns (Fig. 1B) show three reflections ($d_{1\,0\,0}$, $d_{1\,1\,0}$ and $d_{2\,0\,0}$), which satisfy the rules for a *P6mm* symmetry group. Comparing the sharp of the N_2 isotherms in Fig. 1A and the widening of the (1 0 0) peak in Fig. 1B it would be observed that the crystalline order along this plane is hardly changed for all Ti-containing catalysts. This would mean that after Ti-incorporation the structure of SBA-15 material is preserved. The pore size distribution derived from adsorption and desorption branches of N_2 isotherms are shown in Fig. 2A and B, respectively. All oxide catalysts show a narrow BJH pore size distribution centered at 6.5 nm, as derived from the adsorption branch of isotherm (Fig. 2A). The pore size distribution derived from desorption branch show two distinct peaks: the first one, located in the pore width range low 4 nm, indicates the presence of small complementary pores (mainly micropores), and the second one represents the ordered mesopores [33]. Table 1 summarizes specific BET surface area (S_{BET}), total and micropore volume, micropore area and average pore diameter of the pure supports and oxide CoMo catalysts. For all supports, the BET surface area is very high (636–880 m^2/g) and follows the same trend as their pore volume. The ST20 material with the highest Ti-loading has the largest BET surface area among the synthesized supports (880 m^2/g). This suggests that the introduction of a large amount of titanium does not destroy the hexagonal structure of the support. In order to get a clearer view of the occurrence of pore blocking, the BET specific areas of oxide CoMo catalysts were expressed in Table 1 per g of support, as it was proposed by Vradman et al. [34]. The oxide catalysts show BET specific area that is approximately one third that of the respective

Table 1
Labeling and textural properties[a] of the oxide CoMo/Ti-SBA-15 catalysts

Support/catalyst	Labeling	S_{BET}	S_μ	V_{total}	V_μ	D
SBA-15	ST∞	819	182	0.964	0.096	4.7
CoMo/SBA-15	CoMoST∞	260	39	0.437	0.023	5.9
Ti-SBA-$15_{Si/Ti\,=\,80}$	ST80	826	140	1.012	0.073	4.9
CoMo/Ti-SBA-$15_{Si/Ti\,=\,80}$	CoMoST80	240	15	0.459	0.008	6.6
Ti-SBA-$15_{Si/Ti\,=\,60}$	ST60	678	125	0.782	0.065	4.6
CoMo/Ti-SBA-$15_{Si/Ti\,=\,60}$	CoMoST60	281	40	0.515	0.023	6.2
Ti-SBA-$15_{Si/Ti\,=\,40}$	ST40	636	103	0.692	0.053	4.4
CoMo/Ti-SBA-$15_{Si/Ti\,=\,40}$	CoMoST40	266	29	0.463	0.017	5.9
Ti-SBA-$15_{Si/Ti\,=\,20}$	ST20	880	142	1.041	0.073	4.7
CoMo/Ti-SBA-$15_{Si/Ti\,=\,20}$	CoMoST20	294	39	0.491	0.024	5.5

[a] S_{BET}: BET surface area ($m^2/g_{support}$); S_μ: micropore area ($m^2/g_{support}$); V_{total}: adsorption total pore volume (m^3/g); V_μ: micropore volume (m^3/g); D: average pore diameter (nm) calculated from the adsorption branch of the isotherm.

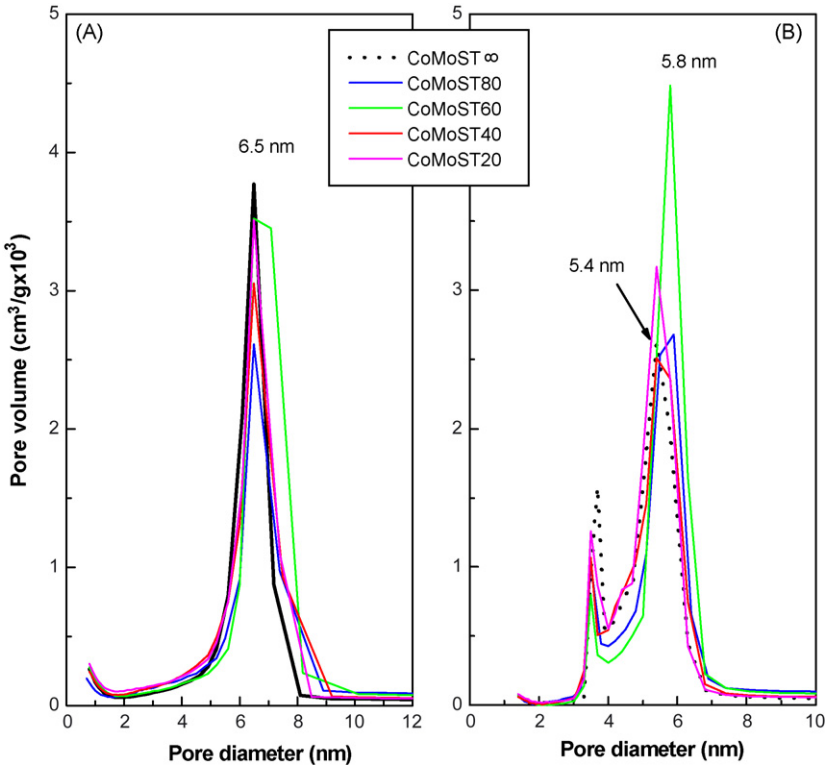

Fig. 2. Pore size distributions for the oxide CoMo/SBA-15 catalysts with and without Ti derived from adsorption (A) and desorption branch (B) of the nitrogen isotherms.

Ti-SBA-15 substrates, but their BET areas still remain high (240–294 m^2/g of support). The oxide CoMoST20 catalyst with the highest Ti-loading has the largest BET surface area among the synthesized CoMo catalysts (294 m^2/g of support). Comparing the total and micropore volume of the catalysts and supports in Table 1, it can be inferred that Co and Mo oxides block the substrate pores, mainly the micropores. This is probably the reason why there is an increase in the average pore diameter after impregnation with CoMo (the microporosity is lost). In short, the textural data of the pure supports and oxide catalysts confirm that Ti incorporation into the SBA-15 material does not destroy the mesoporous structure of this material. There is only a minimal blocking of the host pore systems by the widely dispersed metal oxides located inside the pore system of the SBA-15 material.

In good agreement with a small-angle XRD patterns (Fig. 1B), the TEM images confirmed that hexagonal pore structure of the SBA-15 material was preserved after Ti-incorporation and further metal loading followed by calcination. Micrographs of the oxide CoMoST∞ and CoMoST60 samples with the electron beam parallel to the pore channels are shown in Fig. 3A and B, respectively. As can be seen from those figures, the mesoporous channels of both catalysts are well ordered, with characteristics hexagonal array of uniform channels. From TEM micrographs it can be calculated that the mesopore diameter is about 8.3 nm, which is close to that estimated from the nitrogen sorption isotherms (6.5 nm). Fig. 3C shows the TEM image of CoMoST20 sample with the electron beam perpendicular to the pore channels. The anatase TiO_2 phase was not observed on this and the others TEM images of CoMoST20 sample because the relevant magnification reflects only a very small fraction of material.

Wide-angle power XRD technique was used to investigate the presence of any crystallite species in the catalysts. The X-ray diffraction patterns of the oxide CoMo catalysts are shown in Fig. 4. As seen in this figure, all oxide catalysts reveal typical diffraction patterns, with a single, very broad peak at around 24° 2θ, typical of amorphous silica. Moreover, all catalysts exhibit a high-intensity first peak at ca. 0.82° 2θ and the ensuing low-intensity peaks associated with the SBA-15 hexagonal pore structure, consistent with other studies [33,35–38]. Thus, the mesoporous SBA-15 structure does not undergo major changes after the deposition of Co and Mo oxides, in close agreement with the N_2 adsorption–desorption data commented previously. The XRD patterns of all the catalysts contain a low-intensity peak on the background of the amorphous silica support at around 26.5° 2θ. This peak can be assigned to β-$CoMoO_4$ crystallites (JCPDS No. 21-868) [5]. The low intensity of the peaks indicates that most of the supported species should be widely dispersed on the surfaces of the Ti-free and Ti-containing catalysts. The formation of β-$CoMoO_4$ crystallites on the surface of our catalysts is in close agreement with reported results on cobalt molybdenum oxide supported on silica [39]. The formation of such species indicates that molybdenum species interacting with the support in the oxide Mo/Ti-SBA-15 catalysts could become detached from the siliceous SBA-15 material during consecutive impregnation of the catalysts with cobalt salt solutions. Thus, after calcination at 773 K, molybdenum species in binary CoMo catalysts were partly consumed through the formation of a β-$CoMoO_4$ phase.

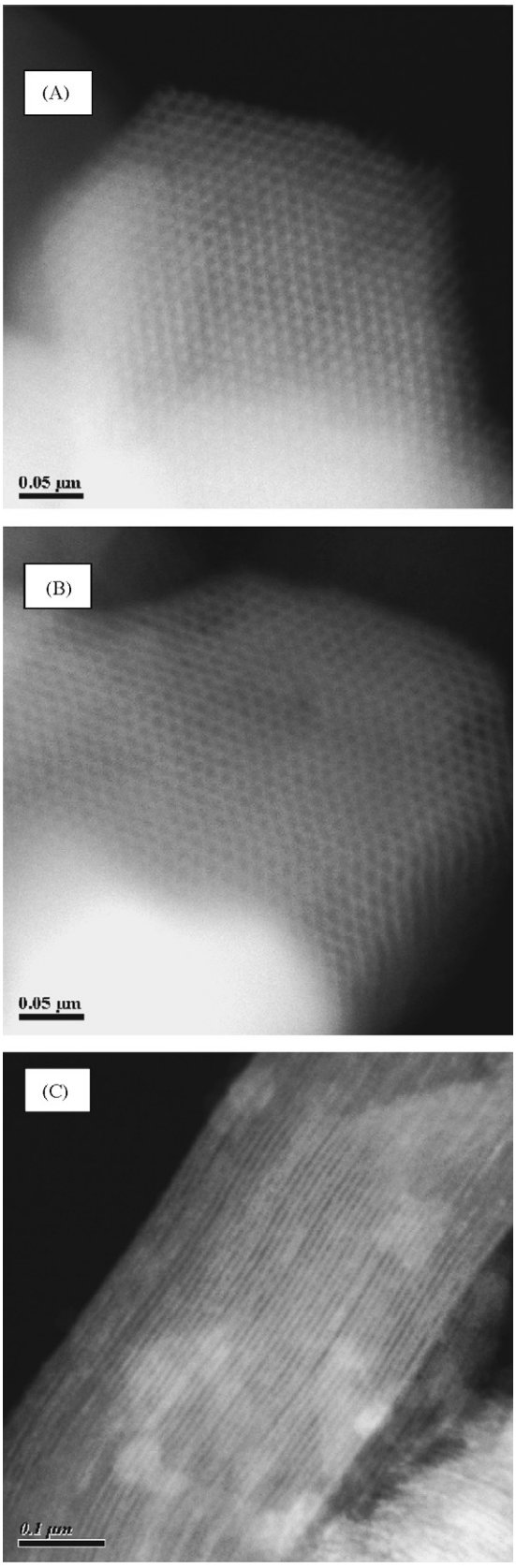

Fig. 3. TEM images of oxide catalysts: (A) CoMoST∞; (B) CoMoST60; (C) CoMoST20.

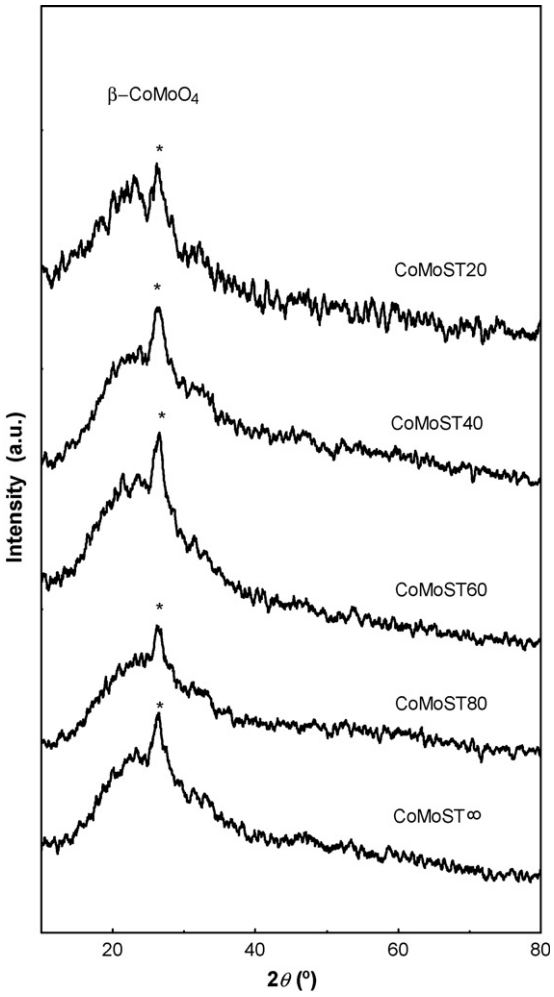

Fig. 4. Wide-angle power X-ray diffraction patterns of oxide CoMo catalysts.

The effect of Ti incorporation into the SBA-15 structure on the type of Co and Mo species formed, as well as on the metal-support and/or Co–Mo interaction, was studied by the TPR technique. The TPR profiles of the oxide systems are shown in Fig. 5A. Regardless of the Ti-content, all catalysts register similar TPR profiles. This means that the Co/Mo species formed are similar for all the catalysts and the Ti-incorporation into the SBA-15 material did not involve further changes in the metal-support interaction (MSI). The TPR profiles of the CoMo catalysts display a single narrow peak at 796 K and another broad one between 850 and 1080 K. Considering the Raman data discussed below, the former could be due to the reduction of octahedrally coordinated polymeric MoO_3 crystallites and/or the $Mo_7O_{24}^{6-}$ phase into MoO_2, whereas the second very broad peak could be ascribed to the second reduction step of those partly reduced MoO_2 phase into Mo metal. This peak may also include the reduction of cobalt–molybdate-like species, as the presence of this structure is derived from the electronic spectra (see below).

The determination of the metal-support interaction is very important in catalysis since the strong-metal support interaction (SMSI) hinders the reduction of oxide species, and in turn hampers their sulfidation. On the other hand, and in the absence

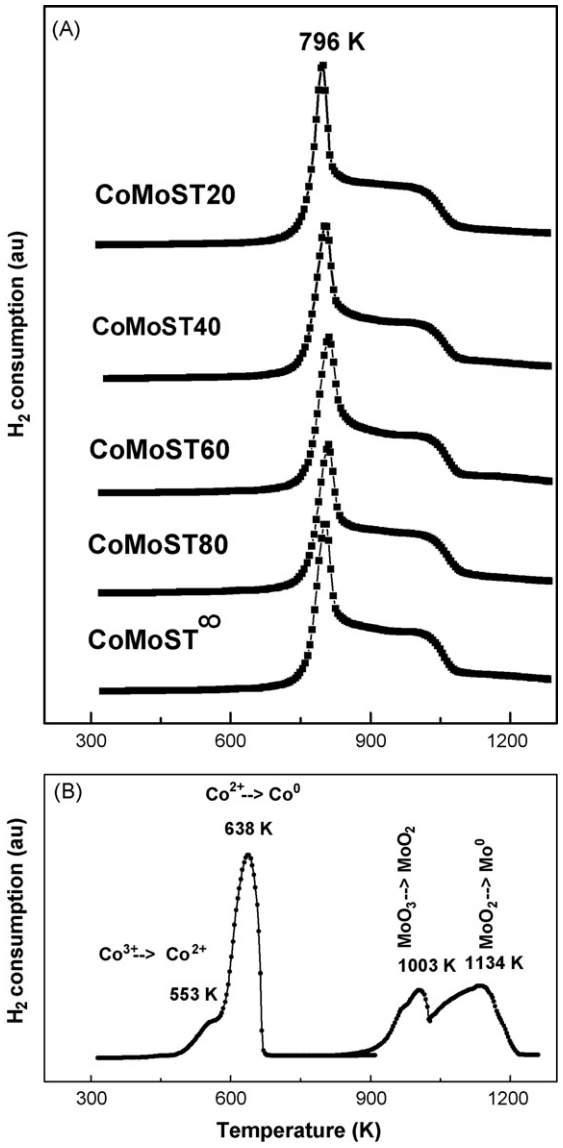

Fig. 5. TPR profiles for oxide catalysts (A) and the bulk Co_2O_3 and MoO_3 compounds (B).

of SMSI, the reduction temperatures of cobalt and molybdenum species might be expected to occur close to those of the respective bulk compounds. To illustrate the existence of a metal-support interaction, the TPR profiles of the bulk Co_2O_3 and MoO_3 compounds are also shown in Fig. 5B. In this figure, the peaks with maxima at 533 and 638 K can be ascribed to a two-step reduction: Co^{3+} to Co^{2+} and Co^{2+} to Co^0, respectively, whereas the reduction profile of the bulk MoO_3 records peak maxima at 1003 and 1134 K (Fig. 5B), which corresponds to the two-step reduction of MoO_3 ($MoO_3 \rightarrow MoO_2 \rightarrow Mo^0$) [40,41]. It is noteworthy that, as a consequence of the molybdenum oxide-support interaction, the reduction temperature of Mo oxide species was extended over a broad temperature interval starting from ca. 800 K, indicating that the molybdenum species are highly dispersed on the support.

The DRS spectra of pure supports and oxide CoMo samples are displayed in Fig. 6A and B, respectively. As seen in Fig. 6A, all Ti-containing materials exhibit one strong band at around 210 nm. According to the literature [32,42], the charge transfer around 210–220 nm could characterize isolated, tetrahedrally coordinated Ti species. Additionally, the spectrum of ST20 support shows a weak broad band centered at 310 nm, which is usually assigned to anatase TiO_2 nanoparticles [32]. However, the absence of significant absorptions above 360–370 nm might be considered as indicative that bulk anatase has not been formed during titanium incorporation [32,43]. All oxide CoMo catalysts display similar electronic spectra (Fig. 6B). The spectrum of each support was subtracted from the spectrum of the corresponding CoMo catalyst. A strong band at about 327 nm has been assigned to an O^{2-}–Mo^{6+} ligand-to-metal charge transfer transition (LMCT) in octahedral coordination [44]. It is noteworthy that no bands are observed located around 250 nm, which are assigned to O^{2-}–Mo^{6+} LMCT in tetrahedral coordination [44]. These results indicate that the dominant species present in the samples are Mo^{6+}-ions in octahedral coordination. The visible part of the spectra displays a broad band in the 450–650 nm region, which can be ascribed to *d–d* transitions ($^4T_{2g}$ to $^4A_{2g}$ and $^4T_{2g}$ to $^4T_{1g}$ (P)) of high spin octahedral Co complexes [45]. The spectra are very similar to that of $CoMoO_4$, in which cobalt ions are placed in an octahedral environment [46]. It may therefore be concluded from the UV–vis spectra that most of the Co interacts with Mo to form the $CoMoO_4$ phase, in good agreement with the X-ray diffraction results. The spectra do not show the band in the 600–800 nm regions, indicating the absence of Co_3O_4 oxide [47].

The Raman spectra of the oxide catalysts are shown in Fig. 7. A main peak at around 941 cm^{-1} stems from the symmetric stretching of the Mo=O bond in bridged or two-dimensional polymeric forms of octahedrally coordinated Mo oxide species, which could be attributed to $Mo_7O_{24}^{6-}$ species [48,49]. Such Mo oxide species are considered to interact weakly on the supports, resulting in higher reducibility and activity in HDS reactions [48,49]. The CoMoST60 and CoMoST20 samples show this main peak (941 cm^{-1}) with the highest intensity. Shoulders at around 868, 816 and 688 cm^{-1} are observed for all catalysts; the former peak reflects the Mo–O–Co stretching vibrations in cobalt–molybdate-like species [48], whereas the latter two reflect Mo–O–Mo linkage in the orthorhombic MoO_3 [48,50], indicating the presence of small amounts of polymerized Mo-oxide on the supports.

3.2. Characterization of sulfided catalysts

Since the active phases in the HDS of the DBT reaction are metal sulfides, the oxide catalysts were sulfided at 673 K and their acid properties were examined by the FTIR spectroscopy of chemisorbed pyridine. The IR spectra of the freshly sulfided catalysts are depicted in Fig. 8. All spectra record bands at ca. 1449 (very strong), 1488 (weak), 1579 cm^{-1} (very weak) and 1609 cm^{-1} (very weak), arising from pyridine adsorbed on Lewis acid sites [51]. No correlation was found between the area of the 1609 cm^{-1} band, which was ascribed to Co^{2+} ions [51], and the surface exposure of non-sulfided Co species (from XPS) discussed below. This may be understood assuming that

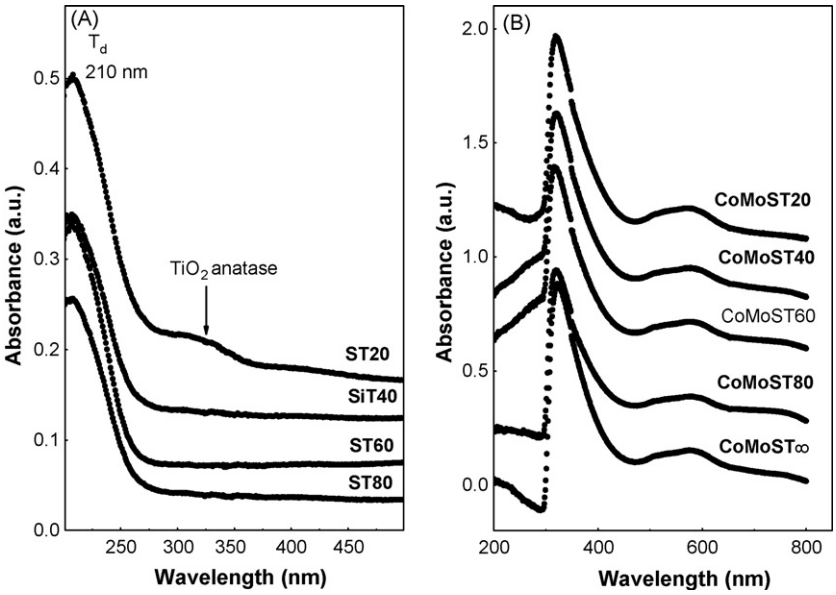

Fig. 6. UV–vis DR spectra of Ti-containing supports (A) and oxide CoMo catalysts (B). The spectrum of each support was subtracted from the spectrum of the corresponding CoMo catalyst.

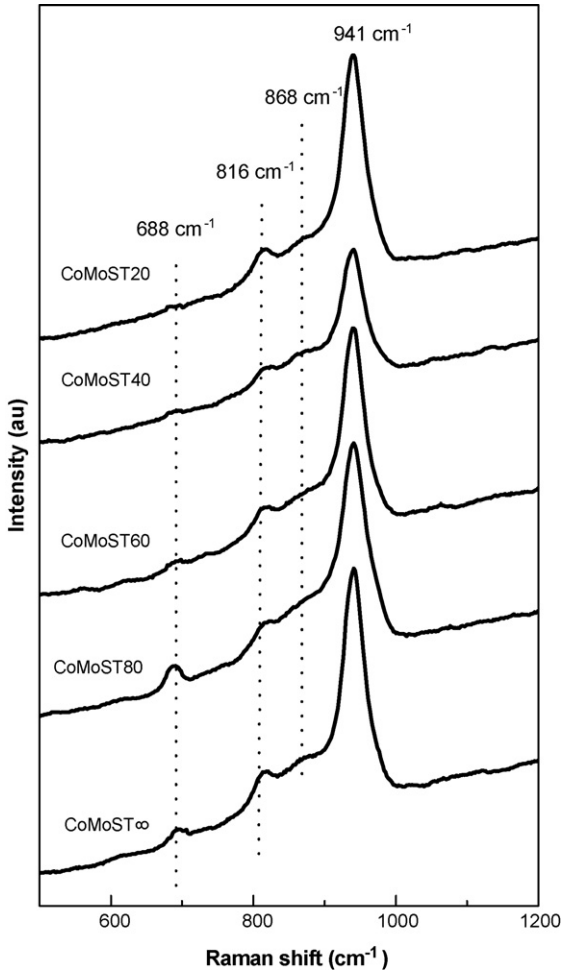

Fig. 7. Raman spectra of oxide CoMo catalysts.

the 1600 cm^{-1} band in the FTIR spectra of adsorbed pyridine does not exclusively come from Co^{2+} ions.

On comparing the areas of the bands, it is clear that the incorporation of Ti into the SBA-15 material enhanced Lewis acidity. This is in good agreement with our previous FTIR study of pyridine adsorption on sulfided CoMo/HMS-Ti catalysts [14]. Since the sulfur vacancies associated with the Co and Mo ions are expected to be of Lewis acid nature, the increase in the Lewis acidity of the Ti-containing samples indicates that the number of sulfur vacancies in those catalysts is higher in comparison to the Ti-free counterpart. The absence of an IR band at 1550 cm^{-1} means that no pyridinium ions (interaction with Brønsted acid site) are formed in either sample. In contrast, our previous study on pyridine adsorbed on sulfided CoMo/Ti-HMS systems revealed the band at 1550 cm^{-1} when Ti-loading was high (Si/Ti = 40) [14] indicating that titania nanodomains exist in five- and six-coordination.

The FTIR spectra of NO chemisorbed on freshly sulfided catalysts are displayed in Fig. 9. Two major bands at around 1866 and 1795 cm^{-1} are observed, together with a very broad band located at 1690 cm^{-1}, in good agreement with previous studies [52–55]. The breakdown of the spectra into Gaussian peaks (not shown here) provides two sets of bands around 1865, 1795, 1790 and 1695 cm^{-1}. The last two bands (1790 and 1695 cm^{-1}) can be assigned to symmetric and anti-symmetric stretching vibrations of NO dimers adsorbed on MoS_2, whereas the doublet bands (1795 and 1865 cm^{-1}) are usually assigned to symmetric and anti-symmetric stretching vibration modes of NO dimers adsorbed on Co sulfide species, respectively [52,54]. It has been established that NO molecules adsorb selectively on the edge or the corner sites of MoS_2 particles rather than on the basal plane or cobalt atoms at the edge of MoS_2 in the CoMoS phase [52]. Thus, for the CoMoST60 sample, the lowest intensity of its broad band at 1695 cm^{-1}

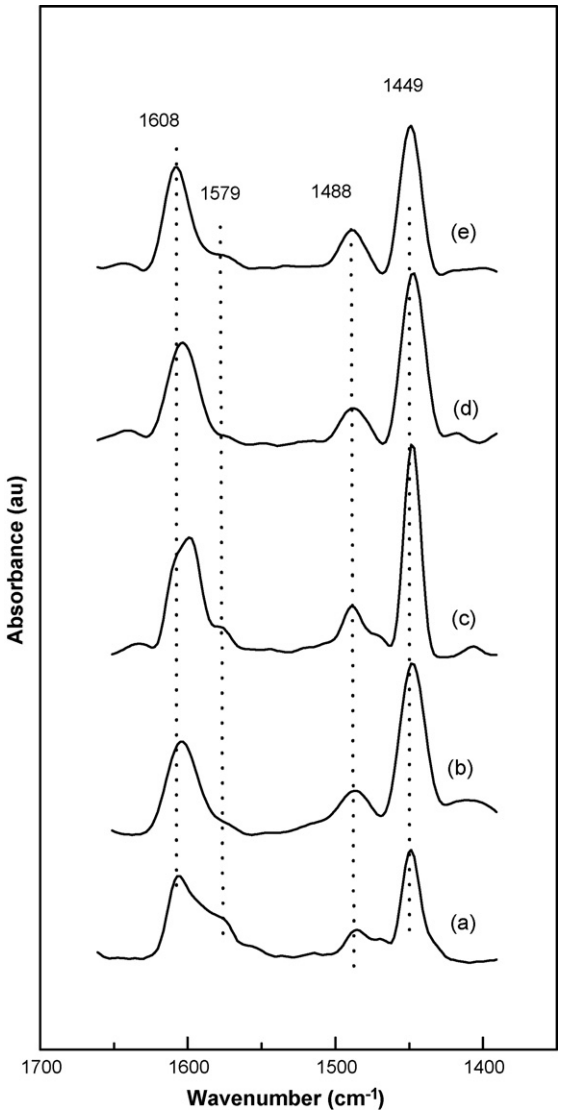

Fig. 8. FTIR spectra of adsorbed (393 K) pyridine on sulfided catalysts: CoMoST∞ (a); CoMoST80 (b); CoMoST60 (c); CoMoST40 (d); CoMoST20 (e).

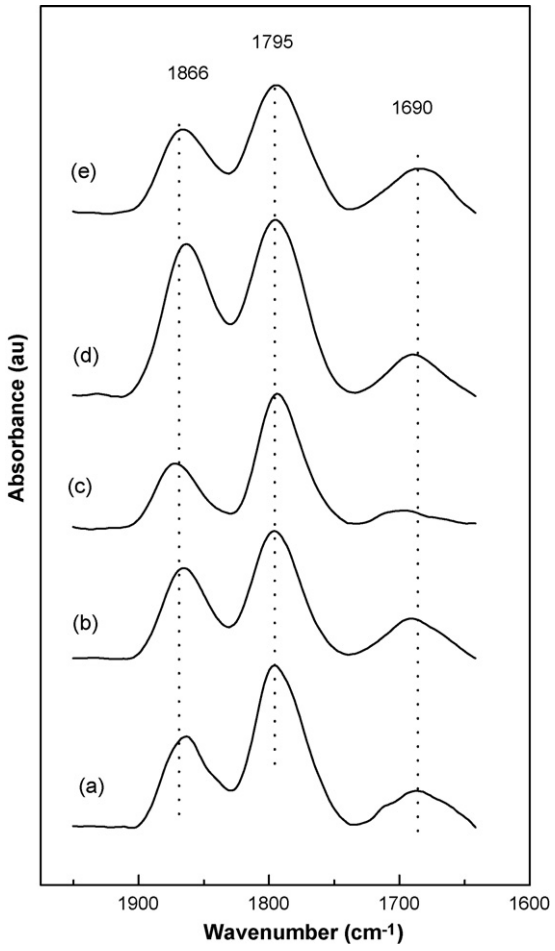

Fig. 9. FTIR spectra of adsorbed NO on sulfided catalysts: CoMoST∞ (a); CoMoST80 (b); CoMoST60 (c); CoMoST40 (d); CoMoST20 (e).

strongly suggests that Co ions are located on the edge sites of MoS_2 slabs. For this catalyst, one may suppose that part of the edge sites of MoS_2 particles accessible to NO adsorption are covered by Co atoms constituting ''Co–Mo–S'' phases. This is consistent with the activity results reported in Fig. 12A, which indicate that this catalyst is the second most active in the HDS of DBT.

The chemical state and surface composition of catalysts following sulfidation at 673 K was revealed by XPS. Consistent with our previous study on Ti-modified CoMo/HMS systems [12–15], the XPS measurements confirmed that the structures present in the sulfide CoMo/Ti-SBA-15 catalysts are largely determined by those present in the calcined samples. This is because a relatively high sulfidation temperature brings about a transformation in the Co(Mo) supported phases, which cannot, however, completely neutralize the influence of the initial surface Mo speciation on the final structure of the supported Co(Mo) phases [56]. The chemical state and surface composition of the catalysts after sulfidation at 673 K was revealed by XPS. Table 2 shows the binding energies (BE) of S 2p, Ti $2p_{3/2}$, Mo $3d_{5/2}$ and Co $2p_{3/2}$ levels. For all catalysts, the binding energy of S 2p level at 162.1 eV is characteristic of S^{2-} ions. For all Ti-containing catalysts, the BE of Ti $2p_{3/2}$ at 459.8 ± 0.1 eV is indicative of the Ti ions being in a tetrahedral arrangement (Si–O–Ti). Additionally, the sulfided CoMoST20 sample records a Ti $2p_{3/2}$ core level peak at BE of 458.6 eV, which is characteristic of titanium ions in an octahedral (Ti–O–Ti) coordination [57]. Thus, in close agreement with the UV–vis data, the small amount (21%) of polymeric species (and/or clusters) of atomically dispersed titanium are located on the surface of the CoMoST20 sample.

Table 2
Binding energies (eV) of the freshly sulfided CoMo/Ti-SBA-15 catalysts[a]

Sample	Mo 3d	Ti $2p_{3/2}$	S 2p	Co $2p_{3/2}$
CoMoST∞	228.7	–	162.1	778.8 (39), 781.3 (61)
CoMoST80	228.7	459.9	162.1	778.9 (37), 781.4 (63)
CoMoST60	228.8	459.8	162.2	778.8 (45), 781.4 (55)
CoMoST40	228.7	459.7	162.1	778.8 (52), 781.3 (48)
CoMoST20	228.7	458.6 (21), 459.8 (79)	162.1	778.7 (47), 781.3 (53)

[a] % area are given in parentheses.

For all catalysts, the Mo 3d and Co 2p core-level spectra are shown in Fig. 10A and B, respectively. As seen in Fig. 10A, all catalysts show the same binding energy and similar full width at half-maximum (FWHM) of the Mo $3d_{5/2}$ peak. The BE value for Mo $3d_{5/2}$ at 228.7 eV is close to that of $CoMo_2S_4$ species [58]. Thus, the ''CoMoS'' phase, which is commonly accepted to be the most active phase in the HDS reaction, probably occurs. For all catalysts, sulfidation of molybdenum species is complete; however, cobalt is partly sulfided. Curve-fitting of the Co 2p spectra discloses two states, with BE values of 778.8 and 781.3 eV; the latter indicating non-sulfided Co^{2+} ions. The former BE value is higher than that expected for the CoS_2 phase (778.1 eV) [58]. Since the BE of Mo $3d_{5/2}$ level suggests the formation of $CoMo_2S_4$ species, the BE value at ca. 778.8 eV can be ascribed to Co^{2+} ions in the $CoMo_2S_4$ phase. In view of the percentage of Co atoms in the surface layer corresponding to sulfide and oxide Co species (data given in parentheses in Table 2), catalysts with higher Ti-content also register a higher amount of surface cobalt sulfide species than the Ti-free and CoMoST80 samples. This suggests that the sulfidation of Co species is enhanced in the presence of Ti^{4+} sites. Indeed, a linear correlation was found between exposed Ti atoms, measured by the Ti/Si atomic ratio, and exposed cobalt sulfide species, measured by the Co/Si atomic ratio (see Fig. 11).

Table 3
Surface atomic ratios of the freshly sulfided CoMo/Ti-SBA-15 catalysts

Sample	Mo/Si	Co/Si	Co/Si (CoS_2)[a]	Ti/Si	S/(Co + Mo)
CoMoST∞	0.019	0.006	0.0023	0.0	1.53
CoMoST80	0.020	0.007	0.0026	0.011	1.48
CoMoST60	0.021	0.006	0.0027	0.016	1.7
CoMoST40	0.020	0.006	0.0031	0.028	1.63
CoMoST20	0.022	0.008	0.0038	0.081	1.76

[a] ''Co/Si (CoS_2)'' means Co atom associated with the band at 778.8 eV *vs.* Si atom.

Table 3 compiles the Mo/Si, Co/Si, Ti/Si and S/(Mo + Co) surface atomic ratios of the fresh sulfided samples. Mo/Si ratios are close to each other. Similarly, the Co/Si atomic ratio changes very little upon increasing the Ti/Si atomic ratio. Thus, the surface exposure of Mo and Co species on SBA-15 modified with Ti did not change significantly with respect to Ti-free catalyst. For example, the CoMoST20 sample with the largest Ti-content among the catalysts studied shows Mo/Si and Co/Si atomic ratios of 0.022 and 0.008, respectively, whereas for Ti-free CoMoST∞ catalyst the Mo/Si and Co/Si atomic ratios are 0.019 and 0.006, respectively. This may indicate that the presence of Ti species could stabilize the Mo and Co species on the SBA-15 support surface. Finally, considering the S/(Mo + Co) atomic ratio, the sulfidation degree of species

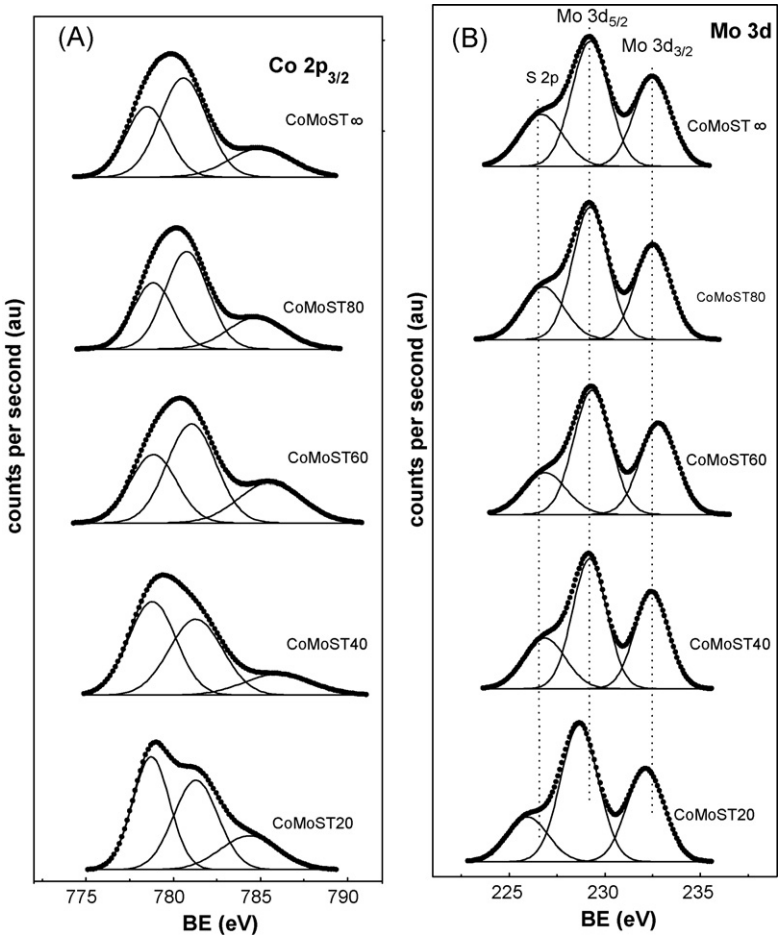

Fig. 10. Mo 3d (A) and Co 2p (B) core-level spectra of the fresh sulfided catalysts.

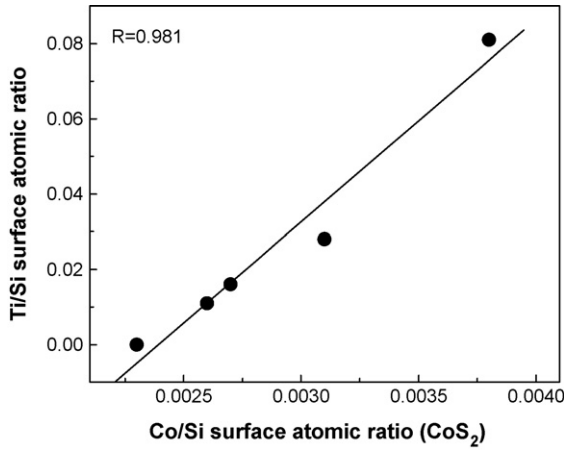

Fig. 11. Correlation between Ti species surface exposures and cobalt sulfide surface exposure (both from Table 2).

follows the order: CoMoST20 > CoMoST60 > CoMoST40 > Ti-free > CoMoST80. Thus, the CoMoST20 catalyst records the highest degree of sulfidation among the catalysts studied but the influence of titanium on the sulfidation degree is not lineal.

3.3. Catalytic activity

The catalytic performance of sulfided CoMo/SBA-15 and CoMo/Ti-SBA-15 samples was studied in the HDS reaction of DBT performed in a batch reactor at 623 K, and under a hydrogen pressure of 3.1 MPa. For all catalysts, the total DBT conversions at 5 h of reaction time are shown in Fig. 12A. With the exception of CoMoST80, Ti-incorporation into the SBA-15 framework had a positive effect on the activity of CoMo systems, and the catalyst with a Si/Ti molar ratio of 20 was the most active in the HDS–DBT reaction. Interestingly, this catalyst records greater activity than a commercial CoMo/Al_2O_3 sample.

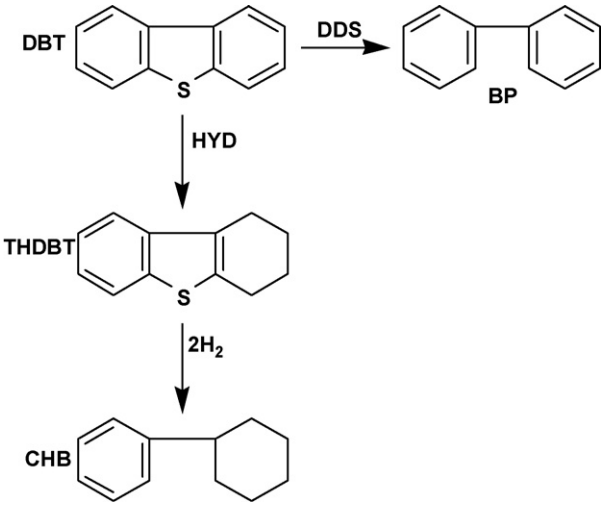

Scheme 1. Reaction scheme for the HDS of DBT over sulfided CoMo/SBA-15 (CoMoST∞) and CoMo/Ti-SBA-15 catalysts: direct desulfurization (DDS), hydrogenation (HYD), dibenzothiophene (DBT), tetrahydrodibenzothiophene (THDBT), biphenyl (BP), cyclohexylbenzene (CHB).

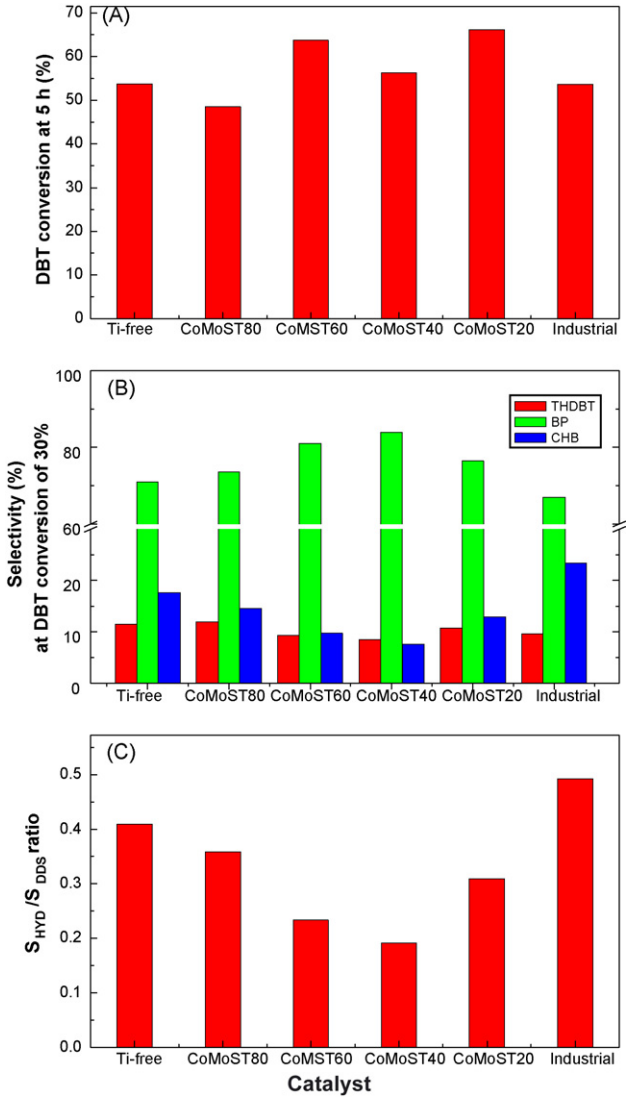

Fig. 12. HDS of DBT: (A) total DBT conversion at 5 h of reaction time, T = 623 K, P = 3.1 MPa; (B) selectivities achieved at a DBT conversion of ca. 30% (T = 623 K, P = 3.1 MPa, different reaction time); (C) S_{HYD}/S_{DDS} selectivity ratio achieved at a DBT conversion of ca. 30% (T = 623 K, P = 3.1 MPa, different reaction time).

The reaction products in the HDS–DBT reaction over CoMo/SBA-15 and CoMo/Ti-SBA-15 catalysts and a commercial CoMo/Al_2O_3 sample were biphenyl (BP), cyclohexylbenzene (CHB) and tetrahydrodibenzothiophene (THDBT). Hydrocracking products such as benzene and cyclohexane were not detected. Fig. 12B shows a comparison of the selectivities of all the catalysts at the same conversion of DBT (about 30%), while Scheme 1 depicts the possible reaction pathways deduced from the products detected. In the HDS of DBT, the prehydrogenation of neighboring phenyl groups led to a THDBT intermediate, after which CHB derivatives are produced (HYD pathway), whereas desulfurization without prehydrogenation afforded BP (DDS pathway). Thus, the HDS of DBT over all the catalysts must proceed through two different pathways: the hydrogenation (HYD) and direct desulfurization (DDS) routes (Scheme 1). Thus, taking account the selectivity data presented in Fig. 12B, the possible reaction

pathways of the DBT transformation under HDS conditions with all the catalysts is depicted in Scheme 1.

Fig. 12C shows the S_{HYD}/S_{DDS} ratios for all the catalysts measured at the same DBT conversions (ca. 30%). Regardless of the Ti-loading, all catalysts show a much lower HYD than DDS, in good agreement with the findings reported in the literature [59]. We thus assume that hydrogenation is a rate-limiting step for the HDS reaction of DBT over CoMo catalysts, as well as for the reference one. As selectivity is linked to the mode of DBT adsorption, the high degree of BP formation indicates that DBT adsorption on the active phase occurs with the DBT molecule standing up in a vertical geometry [60]. This adsorption mode allows the lone pairs in the sulfur to interact with the Lewis sites. Thus, for all catalysts, flat DBT adsorption through the adsorption of π-electrons of the DBT molecule favoring the hydrogenation route of the HDS–DBT reaction appears more difficult than direct C–S bond cleavage. The HYD route in Ti-containing catalysts is inhibited with respect to Ti-free samples.

4. Discussion

4.1. Catalytic activity–structure correlation

Activity tests clearly reveal the larger HDS activity of the Ti-containing catalysts with a Si/Ti ratio lower than 60. The sulfided CoMoST20 catalyst with the greatest Ti-content was the most active among the catalysts studied, followed by the CoMoST60 sample. It is noteworthy that both catalysts record greater activities than a commercial $CoMo/Al_2O_3$ catalyst (Fig. 12A). Catalyst characterization data reveal several aspects of the effect of SBA-15 support modification by Ti: (i) all catalysts have Ti^{4+} ions incorporated in the SBA-15 framework and the CoMoST20 sample is the only one displaying a certain amount of TiO_2 anatase nanoparticles on its surface; (ii) the Ti-free and Ti-containing oxide catalysts reveal similar S_{BET} surface areas and average pore diameters, indicating that the structure of the SBA-15 material is preserved after Ti incorporation; (iii) the Ti-containing sulfide catalysts register a larger Lewis acidity than Ti-free samples (Fig. 8); (iv) after sulfidation at 673 K, none of the catalysts records strong Brønsted acid sites (Fig. 8); and (v) the sample with the highest Ti content (Si/Ti = 20) records the lowest amount of β-$CoMoO_4$ species (Fig. 2). From XPS data of sulfided catalysts, the morphological changes induced by Ti incorporation into the SBA-15 material favor both the surface exposure of the active phase and the degree of Co species sulfidation (Tables 2 and 3).

All catalysts record a linear correlation between the S/(Co + Mo) atomic ratio and total DBT conversion at 5 h of reaction time (Fig. 13A), confirming the importance of the degree of sulfidation of metal species in the HDS activity of the catalysts. The formation of a highly active ‘‘Co–Mo–S’’ phase in all the catalysts is confirmed with XPS by subtracting the BE of the S 2p from the BE of the Co 2p core level (Table 2). For all catalysts, the binding energy difference $\Delta E = 616.7 \pm 0.1$ eV is close to that of 617.0 eV observed when Co species are present mainly in the ‘‘Co–Mo–S’’ phase [61]. Moreover, all catalysts reveal the binding energy difference between the Co 2p and Mo 3d in the 550.1 ± 0.1 eV range. This suggests the presence of cobalt atoms located on the edges of the MoS_2 slabs [61]. For the CoMoST60 sample, which is the second most active among the catalysts studied (Fig. 12A), the location of Co species on the edges of the MoS_2 slabs can be derived from the FTIR spectra of adsorbed NO. For all catalysts, the calculated theoretical bulk Mo/Si and Co/Si atomic ratios are 0.073 and 0.036, respectively. Thus, the comparison of bulk and surface Mo/Si and Co/Si atomic ratios (Table 3) clearly indicates that all catalysts have homogeneously distributed Mo and Co species located mainly within the inner support structure. Accordingly, considering the study of Sampieri et al. [9], the HDS reaction on all catalysts might occur on the active phases located on the support surface, as well as on those active phases located within the inner catalyst pore structure.

The highest activity of the CoMoST20 sample could be linked to the specific characteristics of its pure support. Indeed, besides the Si^{4+} ion substitution by Ti^{4+} ions in the ST20 support, confirmed by UV–vis DR spectroscopy (data not shown here), this catalyst is the only one with TiO_2 anatase nanoparticles located on its surface. Thus, considering the well-documented and more intrinsic activity of Mo species supported on titanium [62], the enhancement of catalytic performance on the CoMoST20 catalyst could be explained by the larger intrinsic activity of the ‘‘Co–Mo–S’’ phase located on TiO_2 nanoparticles. Such preferential location of this phase on TiO_2 rather than on SiO_2 is expected because the isoelectric

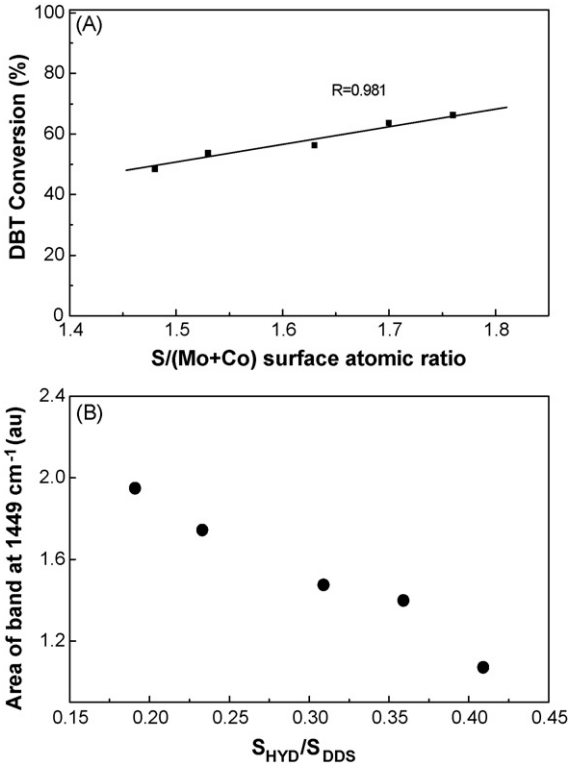

Fig. 13. Relationship between catalytic activity at a reaction time of 5 h and the S/(Co + Mo) atomic ratio of freshly sulfided catalysts (from Table 3) (A) and the correlation between Lewis acidity (Fig. 7) and S_{HYD}/S_{DDS} ratio (from Fig. 12C) (B).

point of TiO_2 is higher than that of SiO_2 [63]. Additionally, the particular characteristics of the most active CoMoST20 catalyst that may to contribute to its higher activity among the catalysts studied are: (i) the greater surface exposure of Co and Mo species among the catalysts studied (Table 3); (ii) inhibition of the formation of β-$CoMoO_4$ phase in its oxide precursor; and (iii) the higher amount of cobalt species having Co^{2+} ions in octahedral coordination (Fig. 6). Indeed, the correlation between the fraction of well-dispersed octahedral cobalt in the oxide precursors and the concentration of the edge sulfur vacancies formed on the active phase of the sulfided samples have been reported previously [56]. Finally, the enhancement of catalytic performance in the CoMoST20 sample could be related to the greater stability of its active phases located on the support surface during the HDS reaction with respect to other catalysts (data no shown here) indicating an enhancement of the metal-support interaction in this catalyst. The enhancement of metal-support interaction after Ti incorporation by grafting into SBA-15 was reported for NiMo catalysts [27].

4.2. Factors influenced the selectivity in HDS of DBT

The large number of studies investigating the nature of the active sites suggests that the hydrogenolysis and hydrogenation reactions occur on separate sites, with the active sites in the desulfurization reaction being coordinately unsaturated sites (CUS) of the metal sulfide. In other words, the hydrogenolysis and hydrogenation would involve Lewis acid sites (vacancies) [64] and Brønsted [65] acid sites, respectively. Taking into account the absence of Brønsted acidity in all synthesized catalysts (Fig. 8), the participation of their Lewis acid sites (vacancies) in the hydrogenolysis reaction is clear. Indeed, the trend of the S_{HYD}/S_{DDS} ratio is opposite to that of Lewis acidity, as determined from the FTIR spectra of adsorbed pyridine (peak at 1449 cm^{-1}) (Fig. 13B). Thus, the enhancement of the DDS route of the HDS–DBT reaction over Ti-containing catalysts with respect to the Ti-free sample is linked to an increase in the number of active sites (CUS) of the metal sulfide caused by Ti incorporation. Moreover, because the hydrogenation of DBT is a steric demanding reaction, a decrease of HYD properties of the CoMo/Ti-SBA-15 catalysts with respect to Ti-free sample may indicate inhibition of the flat DBT adsorption on the active sites. Taking account the different modes of DBT adsorption, Daage and Chianelli [66] proposed that only rim sites of active phase present suitable geometry for adsorbing reactants through aromatic ring whereas the edge sites of this phase are largely responsible for the DDS route of DBT transformation. Assuming this model, the decrease in HYD observed for the Ti-containing CoMo/SBA-15 catalysts with respect to Ti-free CoMo/SBA-15 sample can be probably due to development of a lower amount of rim sites in the active phase.

The presence of both Lewis and Brønsted acid sites on γ-Al_2O_3 has been confirmed by means of NH_3-stepwise temperature-programmed desorption (STPD) [69]. Thus, the largest HYD performance of the commercial $CoMo/Al_2O_3$ sample studied in this work (Fig. 12C) could be explained assuming the participation of their Brønsted acid sites in the heterolytic mechanism of hydrogenation [67]. This reaction mechanism involves the hydrogen activation on the metal sulfide phase followed by a spillover of H-atoms from the sulfide phase to the aromatic ring of the S-compound strongly adsorbed on the acidic site located in the close vicinity of the hydrogenation sites [68]. Assuming this reaction mechanism and the selectivity data presented in Fig. 12B, Scheme 1 shows the possible reaction pathways of the DBT transformation under HDS conditions with the SBA-15-supported catalysts and commercial catalyst.

Contrary to this study, our previous study on the CoMo/Ti-HMS catalysts [12] demonstrated that an increase in HYD raising Ti content in the catalysts was accompanied by a large increase in the Co species surface exposure. Thus, the enhancement of hydrogenation of those catalysts comes from cobalt species confirming that Co is a good hydrogenation catalyst [73]. Other possible explanation of an increase in HYD raising Ti content in the CoMo/Ti-HMS catalysts involves the participation of their Brønsted acid sites in the heterolytic mechanism of hydrogenation. Contrary to the Ti-free CoMo/HMS sample, the sulfided CoMo/Ti-HMS systems with a large Ti content showed Brønsted acidity [12]. Additionally, the formation of new Brønsted acid sites (from –SH groups) upon higher hydrogen pressure than those employed in this study (5.5 MPa *versus* 3.1 MPa of this study) is highly possible. The –SH groups, which are formed on the support surface upon dissociation of H_2S on the CUS sites [70,71], was proposed to have a dual function, i.e., one as Brønsted acid sites providing protons and the other as the source of hydrogen [72].

In short, this study has shown that the CoMoST20 catalyst is more effective for the removal of sulfur during the desulfurization of DBT than a commercial $CoMo/Al_2O_3$ catalyst. The high activity of the CoMoST20 catalyst during the HDS of DBT despite the absence of Brønsted acidity suggests that the CUS sites may be of greater importance in DBT transformation than the Brønsted acid sites, in good agreement with previous reports [74–77]. This is because the electronic effect in the HDS–DBT reaction, which could be induced by acid sites, has been reported as relatively low [74–77].

5. Conclusions

This study shows that the incorporation of Ti into the SBA-15 material was beneficial for catalyst morphology, providing better dispersion for the oxide and sulfide metal species, which in turn favor the sulfidation of cobalt species. The HDS of DBT over all catalysts proceeds via the direct desulfurization route (main route) and hydrogenation (HYD) pathway. The incorporation of Ti into the SBA-15 afforded catalysts that are more active than the Ti-free counterpart because they enhance the DDS route.

The presence of a small amount of TiO_2 anatase phase at the surface of the CoMoST20 catalyst was found to be beneficial for the desulfurization properties of the SBA-15-supported CoMo catalyst. This material presents homogeneous active

phase dispersion and its modification by Ti leads to an enhancement of the degree of sulfidation of Co species and also elicits the formation of a larger number of CUS sites, which prove to be the main factors influencing S removal during the HDS of DBT.

Acknowledgements

The authors would like to express their gratitude to Project IN118002 for its financial support. Thanks are due to Eng. M. Hernandez, Dr. J. Arenas and Dr. M. Lardizabal for technical assistance.

References

[1] EP directive 2003/17/EC, Off. J. Eur. Union L 76, 46 (2003) 10.
[2] C. Song, Catal. Today 77 (2002) 17.
[3] S.K. Maity, B.N. Srinivas, V.V.D.N. Prasad, A. Singh, G. Murali Dhar, T.S.R. Prasada Rao, in: T.S.R. Prasada Rao, G. Murali Dhar (Eds.), Recent Advances in Basic and Applied Aspects of Industrial Catalysis, Stud. Surf. Sci. Catal. 113 (1998) 579.
[4] C. Song, K.M. Reddy, Prep. Am. Chem. Soc. Div. Petro. Chem. 41 (1996) 567.
[5] A. Wang, Y. Wang, T. Kabe, Y. Chen, A. Ishihara, W. Qian, J. Catal. 199 (2001) 19.
[6] A. Wang, Y. Wang, T. Kabe, Y. Chen, A. Ishihava, W. Qian, P. Yao, J. Catal. 210 (2002) 319.
[7] T. Klimova, M. Calderon, J. Ramirez, Appl. Catal. A: Gen. 240 (2003) 29.
[8] U.T. Turaga, C. Song, Catal. Today 86 (2003) 129.
[9] A. Sampieri, S. Pronier, J. Blanchard, M. Breysse, S. Brunet, K. Fajerwerg, C. Louis, G. Pérot, Catal. Today 107/108 (2005) 537.
[10] T. Halachev, R. Nava, L. Dimitrov, Appl. Catal. A: Gen. 169 (1998) 111.
[11] T. Halachev, J.A. de los Reyes, C. Aranjo, G. Cordoba, L. Dimitrov, in: B. Delmon, G.F. Froment, P. Grange (Eds.), Hydrotreatment and Hydrocracking of Oil Fractions, Stud. Surf. Sci. Catal. 127 (1999) 401.
[12] T.A. Zepeda, T. Halachev, B. Pawelec, R. Nava, T. Klimova, G.A. Fuentes, J.L.G. Fierro, Chem. Mater. 17 (2005) 4062.
[13] T.A. Zepeda, T. Halachev, B. Pawelec, R. Nava, T. Klimova, G.A. Fuentes, J.L.G. Fierro, Catal. Commun. 7 (2006) 33.
[14] T.A. Zepeda, B. Pawelec, J.L.G. Fierro, T. Halachev, J. Catal. 242 (2) (2006) 254.
[15] T.A. Zepeda, B. Pawelec, J.L.G. Fierro, T. Halachev, Appl. Catal. B: Environ. 71 (2007) 223.
[16] B. Pawelec, S. Damyanova, R. Mariscal, J.L.G. Fierro, I. Sobrados, J. Sanz, L. Petrov, J. Catal. 223 (2004) 86.
[17] G. Murali Dhar, G. Muthu Kumaran, Manoj Kumar, K.S. Rawat, L.D. Sharma, B. David Raju, K.S. Rama Rao, Catal. Today 99 (3/4) (2005) 309.
[18] L. Vradman, M.V. Landau, M. Herskowitz, V. Ezersky, M. Talianker, S. Nikitenko, Y. Koltypin, A. Gedanken, J. Catal. 213 (2003) 163.
[19] T. Klimova, L. Lizama, J.C. Amezcua, P. Roquero, E. Torrés, J. Navarrete, J.M. Domínguez, Catal. Today 98 (2004) 141.
[20] J.C. Amezcua, L. Lizama, C. Salcedo, I. Puente, J.M. Domínguez, T. Klimova, Catal. Today 107/108 (2005) 578.
[21] G. Murali Dhar, B.N. Srinivas, M.S. Rana, M. Kumar, S.K. Maity, Catal. Today 86 (2003) 45.
[22] M. Breysse, P. Afanasiev, C. Geantet, M. Vrinat, Catal. Today 86 (2003) 5.
[23] D.Y. Zhao, Q.S. Huo, J.L. Feng, B.F. Chmelka, G.D. Stucky, J. Am. Chem. Soc. 120 (1998) 6024.
[24] D. Zhao, J. Feng, Q. Huo, N. Melosh, G.H. Fredrickson, B.F. Chmelka, G.D. Stucky, Science 279 (1998) 548.
[25] H. Shimada, Catal. Today 86 (2003) 17.
[26] S. Yoshinaka, K. Segawa, Catal. Today 45 (1998) 293.
[27] O.Y. Gutiérrez, G.A. Fuentes, C. Salcedo, T. Klimova, Catal. Today 116 (4) (2006) 485.
[28] T. Klimova, L. Lizama, J.C. Amezcua, P. Roquero, E. Terrés, J. Navarrete, J.M. Domínguez, Catal. Today 98 (2004) 141.
[29] K. Flodström, V. Alfredsson, Micropor. Mesopor. Mater. 59 (2003) 167.
[30] C.D. Wagner, W.M. Riggs, L.E. Davis, J.F. Moulder, G.E. Muilenberg, Handbook of X-ray Photoelectron Spectroscopy, Perkin-Elmer Corp., 1979.
[31] F. Schüth, A. Wingen, J. Saver, Micropor. Mesopor. Mater. 44/45 (2001) 465.
[32] A. Tuel, L.G. Hubert-Pfalzgraf, J. Catal. 217 (2003) 343.
[33] M. Kruk, M. Jaroniec, C.H. Ko, R. Ryoo, Chem. Mater. 12 (2000) 1961.
[34] L. Vradman, M.V. Landau, D. Kantorovich, Y. Koltypin, A. Gedanken, Micropor. Mesopor. Mater. 79 (2005) 307.
[35] Z. Luan, E.M. Maes, P.A.W. van der Heide, D. Zhao, R.S. Czernuszewicz, L. Kevan, Chem. Mater. 11 (1999) 3680.
[36] D. Zhao, J. Sun, Q. Li, G.D. Stucky, Chem. Mater. 12 (2000) 275.
[37] Y. Wang, M. Noguchi, Y. Takahashi, Y. Ohtsuka, Catal. Today 68 (2001) 3.
[38] K.R. Sawant, R.F. Lobo, Stud. Surf. Sci. Catal. 141 (2002) 53.
[39] A.M. Venezia, V. La Parola, G. Deganello, D. Cauzzi, G. Leonardo, G. Predieri, Appl. Catal. A: Gen. 229 (1/2) (2002) 261.
[40] S. Damyanova, L. Petrov, M.A. Centeno, P. Grange, Appl. Catal. A: Gen. 224 (2002) 271.
[41] P. Arnoldy, M.C. Franken, B. Scheffer, J.A. Moulijn, J. Catal. 96 (1985) 381.
[42] B. Notari, Adv. Catal. 41 (1996) 253.
[43] S. Klein, B.M. Veckhuysen, J.A. Martens, W.F. Maier, P.A. Jacobs, J. Catal. 163 (1996) 489.
[44] R.A. Schoonheydt, Diffuse reflectance spectroscopy, in: F. Delannay (Ed.), Characterization of Heterogeneous Catalysts, Marcel Dekker, New York, 1984, p. 125.
[45] P. Gajardo, P. Grange, B. Delmon, J. Phys. Chem. 83 (1979) 1771.
[46] J.E. Herrera, D.E. Resasco, J. Catal. 221 (2004) 354.
[47] H.K. Matralis, Ch. Papadopoulou, A. Lycourghiotis, Appl. Catal. A: Gen. 116 (1994) 221.
[48] N. Kunisada, K.-H. Choi, Y. Korai, I. Mochida, N. Nakano, Appl. Catal. A: Gen. 269 (2004) 43.
[49] K.-H. Choi, Y. Korai, I. Mochida, Appl. Catal. A: Gen. 260 (2004) 229.
[50] Z. Li, Y. Fu, J. Bao, M. Jiang, T. Hu, T. Liu, Y.-N. Xie, Appl. Catal. A: Gen. 220 (2001) 21.
[51] T.I. Korányi, F. Moreau, V.V. Rozanov, E.A. Rozanova, J. Mol. Struct. 103 (1997) 410.
[52] N.Y. Topsøe, H. Topsøe, J. Catal. 84 (1983) 386.
[53] B. Pawelec, R. Navarro, J.L.G. Fierro, P.T. Vasudevan, Appl. Catal. A: Gen. 168 (1998) 205.
[54] J.L.G. Fierro, in: J.L.G. Fierro (Ed.), Spectroscopic Characterization of Heterogeneous Catalysts, Part B, Elsevier Science Publishers, Amsterdam, 1990, p. B67.
[55] A. Arteaga, J.L.G. Fierro, F. Delanny, B. Delmon, Appl. Catal. A: Gen. 26 (1986) 227.
[56] Ch. Papadopoulou, J. Vakros, H.K. Matralis, Ch. Kordulis, A. Lycourghiotis, J. Colloid Interface Sci. 261 (2003) 146.
[57] M.C. Capel-Sanchez, J.M. Campos-Martin, J.L.G. Fierro, M.P. De Frutos, A. Padilla Polo, Chem. Commun. (2000) 855.
[58] D. Briggs, M.P. Seah (Eds.), Practical Surface Analysis. Auger and X-ray Photoelectron Spectroscopy, Wiley, New York/Salle and Sauerländer, 1990.
[59] F. Bataille, J.-L. Lemberton, P. Michaud, G. Pérot, M. Vrinat, M. Lemaire, E. Schulz, M. Breysse, S. Kasztelan, J. Catal. 191 (2) (2000) 409.
[60] H. Farag, K. Sakanishi, M. Kouzu, A. Matsumura, Y. Sugimoto, I. Saito, Catal. Commun. 4 (2003) 321.
[61] I. Alstrup, I. Chorkendoref, R. Candia, B.S. Clausen, H. Topsoe, J. Catal. 77 (1982) 397.
[62] P. Schacht, G. Hernández, L. Cedeño, J.H. Mendoza, S. Ramírez, L. García, J. Ancheyta, Energy Fuels 17 (2003) 81.
[63] G.A. Parks, Chem. Rev. 65 (1965) 177.
[64] J.M.J.G. Lipsch, G.C.A. Schuit, J. Catal. 15 (1969) 179.
[65] M. Nagai, T. Sato, A. Aiba, J. Catal. 97 (1986) 52.
[66] M. Daage, R.R. Chianelli, J. Catal. 149 (1994) 414.

[67] Y. Okamoto, A. Maezawa, T. Imanaka, J. Catal. 120 (1989) 29.
[68] M. Breysse, E. Furimsky, S. Kasztelan, M. Lacroix, G. Perot, Catal. Rev.-Sci. Eng. 44 (4) (2002) 651.
[69] W. Zhang, P.G. Smirniotis, Appl. Catal. A: Gen. 168 (1998) 113.
[70] S.M. Riseman, S. Bandyopadhyay, F.E. Massoth, E.M. Eyring, Appl. Catal. 16 (1985) 29.
[71] N.-Y. Topsøe, H. Topsøe, F.E. Massoth, J. Catal. 119 (1989) 252.
[72] N.-Y. Topsøe, H. Topsøe, J. Catal. 139 (1993) 641.
[73] M. Kurhinem, T.A. Pakkanen, Appl. Catal. A: Gen. 192 (2000) 97.
[74] H. Topsøe, B.S. Clausen, R. Candia, C. Wivel, S. Mørup, J. Catal. 68 (1981) 433.
[75] G. Perot, Catal. Today 86 (2003) 111.
[76] E. Lecrenay, K. Sakanishi, T. Nagamatsu, I. Mochida, T. Suzuka, Appl. Catal. B: Environ. 18 (1998) 325.
[77] N. Kunisada, K.-H. Choi, Y. Korai, I. Mochida, K. Nakano, Appl. Catal. A: Gen. 276 (2004) 51.